

FULL PAPER

Open Access



# Geographical and seasonal variations of gravity wave activities in the upper mesosphere measured by space-borne imaging of molecular oxygen nightglow

Yuta Hozumi<sup>1,2,3\*</sup> , Akinori Saito<sup>4\*</sup>, Takeshi Sakanoi<sup>5</sup>, Jia Yue<sup>2,3</sup>, Atsushi Yamazaki<sup>6</sup> and Hanli Liu<sup>7</sup>

## Abstract

Geographical and seasonal variations of gravity wave events in the upper mesosphere were investigated using the nightglow imaging data obtained by the Visible and near-Infrared Spectral Imager (VISI) on the Ionosphere, Mesosphere, upper Atmosphere and Plasmasphere (IMAP) onboard the International Space Station (ISS). The nadir-imaging data of the O<sub>2</sub>(0–0) atmospheric band (762 nm) with the typical emission peak around 95 km altitude was used to investigate small-scale waves (horizontal wavelengths less than ~200 km) on a global scale. To detect gravity wave events, the variance of high-pass filtered nightglow images within a local 100 km radius was evaluated, with a threshold set at three times the standard deviation from the average variance of the background level. A data screening algorithm that evaluates the variance of upwelling contamination light emission was also introduced to remove contaminated data. Applying the variance filter and data screening algorithm to a nearly 3-year data set, from November 2012 to August 2015, occurrence maps of wave events for four seasons were derived. The occurrence maps show a higher frequency of wave events in winter high latitudes (>40° N/S), considerably attributed to gravity wave activity associated with the polar night jet. Hot spots were observed near orographic sources in winter high latitudes, including the eastern part of North America, Europe, and the southern Andes. In the summer hemisphere, hot spots were detected at mid-to-high latitudes such as North America, Europe, and the eastern side of the Eurasian continent, and at equatorial latitudes just above the intertropical convection zone (ITCZ). They are likely gravity waves from deep convection that arise from mid-latitude summertime thunderstorms and the ITCZ, respectively. During the equinox seasons, hot spots were detected near convective sources such as the Amazon Rainforest, Congo Rainforest, and the Indochina peninsula.

**Keywords** Mesospheric gravity waves, Gravity wave climatology, Nadir-viewing airglow observation

\*Correspondence:

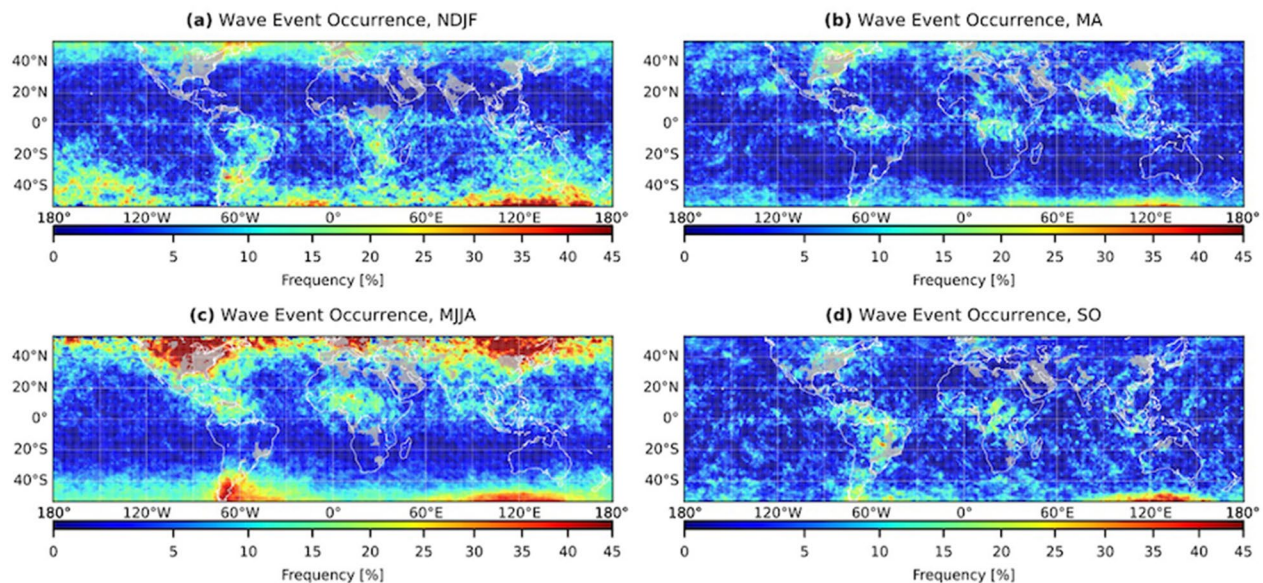
Yuta Hozumi  
yuta.hozumi@nasa.gov  
Akinori Saito  
saitoua@kugi.kyoto-u.ac.jp

Full list of author information is available at the end of the article



© The Author(s) 2024. **Open Access** This article is licensed under a Creative Commons Attribution 4.0 International License, which permits use, sharing, adaptation, distribution and reproduction in any medium or format, as long as you give appropriate credit to the original author(s) and the source, provide a link to the Creative Commons licence, and indicate if changes were made. The images or other third party material in this article are included in the article's Creative Commons licence, unless indicated otherwise in a credit line to the material. If material is not included in the article's Creative Commons licence and your intended use is not permitted by statutory regulation or exceeds the permitted use, you will need to obtain permission directly from the copyright holder. To view a copy of this licence, visit <http://creativecommons.org/licenses/by/4.0/>.

## Graphical Abstract



## Introduction

Atmospheric gravity waves are excited by various sources, such as convection activity (Alexander and Pfister 1995), topography (Nastrom and Fritts 1992; Eckermann and Preusse 1999), fronts, and geostrophic adjustment (e.g., Plougonven and Zhang 2014), etc. They propagate upward in Earth's atmosphere and decelerate or accelerate background wind via their dissipation process. The gravity wave forcing essentially contributes to the atmospheric circulations, the thermal structure, and the distribution of chemical components (Lindzen 1981; Holton 1982, 1983; Fritts and Alexander 2003).

A number of studies on gravity waves have been conducted with theoretical consideration, numerical simulations, and various observations both from the ground and space. Space-borne observations provide an excellent opportunity to study gravity waves in the middle and upper atmosphere on a global scale. Historically, limb and occultation experiments, such as the Limb Infrared Monitor of the Stratosphere (LIMS) (Fetzer and Gille 1994), Global Positioning System (GPS) Radio Occultations (Tsuda et al. 2000), the Cryogenic Infrared Spectrometers and Telescopes for the Atmosphere (CRISTA) (Ern 2004), the Microwave Limb Sounder (MLS) (Wu and Eckermann 2008), the High Resolution Dynamics Limb Sounder (HIRDLS) (Alexander et al. 2008), and the Sounding of the Atmosphere using Broadband Emission Radiometry (SABER) (Preusse et al. 2009; Ern et al.

2011), lead to global measurements of gravity waves. Because of their viewing geometry, they have good vertical resolution and sensitivity to gravity waves with short vertical wavelengths, but their sensitivity to waves of short horizontal wavelengths is limited. For example, SABER measures waves with horizontal wavelengths longer than  $\sim 200$  km. In contrast, nadir-viewing instruments have good horizontal resolution and are sensitive to gravity waves with short horizontal wavelengths. The Atmospheric Infrared Sounder (AIRS) aboard the Aqua satellite and The Cloud Imaging and Particle Size (CIPS) instrument on the AIM satellite have revealed the characteristics of stratospheric gravity waves on a global scale (Hoffmann et al. 2013; Ern et al. 2017; Randall et al. 2017; Forbes et al. 2021).

In the mesosphere, however, the global morphology of gravity wave activities has been rarely studied using nadir-viewing instruments compared to waves at lower altitudes. Consequently, the global view of gravity waves with short horizontal wavelengths in the mesosphere is poorly examined or unknown from observations. The Day–Night Band (DNB) on the Visible/Infrared Imaging Radiometer Suite (VIIRS) onboard the Suomi National Polar-orbiting Partnership (Suomi NPP) satellite and NOAA20 satellite and the Visible and near-Infrared Spectral Imager (VISI) on the Ionosphere, Mesosphere, upper Atmosphere and Plasmasphere (IMAP) carried on the International Space Station (ISS) have the capability

to detect gravity waves in the upper mesosphere with high horizontal resolution. They have sensitivity to gravity waves with short horizontal wavelengths (less than  $\sim 100$  km). VIIRS/DNB has resolved detailed structures of mesospheric gravity waves at a sub-kilometric scale (Miller et al. 2012, 2015). Because the DNB is a broadband sensor (505–890 nm), it is severely contaminated by emissions from the lower atmosphere, such as city lights, orographic features like snowy mountains, and reflection from cloud tops, making it extremely difficult to conduct a comprehensive global morphology study. The VISI O<sub>2</sub>(0-0) atmospheric band measurement of gravity waves at 762 nm is less interfered by background contaminations from below because of the strong absorption of O<sub>2</sub> between the troposphere and mesopause, and is preferable for global morphology or climatology studies of mesospheric gravity waves (Yue et al. 2019). VISI's O<sub>2</sub>(0-0) band data have been used for global statistical studies for concentric gravity waves (Perwitasari et al. 2016) and mesospheric bores (Hozumi et al. 2019). However, these studies have focused only on certain waves or features with special shapes, and their event surveys were based on visual inspections.

A global study on more general gravity wave activity, regardless of their shapes, is required to understand mesospheric gravity waves better. In this study, we developed a wave event detection algorithm using the VISI O<sub>2</sub>(0-0) band data and derived global occurrence maps of wave events to investigate geographical and seasonal variations in wave activity at the altitude of the upper  $\sim 95$  km.

This paper is organized as follows: “**Instrumentation and observations**” section briefly introduces the mesospheric airglow measurements of VISI. The methodologies of wave event detection and data screening are described in “**Methodology**” section. “**Results**” section presents the results of the wave occurrence analysis. “**Discussion**” section discusses some interesting features observed in the occurrence maps. “**Summary**” section summarizes the study.

### Instrumentation and observations

The VISI is a visible and near-infrared spectral imager, one of the two imagers of the Ionosphere, Mesosphere, upper Atmosphere and Plasmasphere mapping mission onboard the International Space Station (ISS-IMAP mission, Sakanoi et al. 2011). The VISI observes airglow in the mesosphere and ionosphere on the night side of the Earth, including the O<sub>2</sub>(0-0) atmospheric band (762 nm), the OH Meinel band (730 nm), and the OI band (630 nm). The O<sub>2</sub>(0-0) atmospheric band data from the VISI are utilized in this study. The typical peak altitude of O<sub>2</sub>(0-0) atmospheric band is  $\sim 95$  km, and its

1/e width is  $\sim 5$  km (Burrage et al. 1994; Yee et al. 1997). VISI's O<sub>2</sub>(0-0) band is sensitive to gravity waves with vertical wavelengths longer than  $\sim 10$  km.

The instrumentation of the VISI is briefly introduced here. The VISI is a grism imaging spectrometer that consists of a fast and distortion-free objective lens (F/0.96), two line slits, collimator and camera optics, and a CCD sensor. The VISI has two slit-shaped field-of-views (FOVs) perpendicular to the ISS orbit track, pointing 45° forward and 45° backward to the nadir. The incident lights from forward and backward FOVs pass through the respective slits, are dispersed by a grism, and focus on the different areas of the CCD detector. One axis of the CCD corresponds to space perpendicular to the orbit track. The other axis of the CCD corresponds to wavelengths and the difference in FOVs. Further details on the instrumentation of the VISI are described in Sakanoi et al. (2011).

During nominal operations of the VISI, not all pixel data of the CCD were downlinked; only segments of count data near the emission peak lines in the wavelength axis of the CCD were downlinked. The VISI has mainly two observation modes: the spectral mode and the peak mode. In the spectral mode, count data in the 12-row lines near the emission peaks are downlinked (the emission peaks are nominally the O<sub>2</sub>(0-0) atmospheric band, the OH Meinel band, and the OI band). In the peak mode, only the maximum (peak) count and minimum (bottom) count in the 12-row lines in each column are downlinked. Figure 1 shows an example of the spectral and peak mode data for the O<sub>2</sub>(0-0) atmospheric band (762 nm) obtained at 1803UT on April 16, 2018. To minimize telemetry data size, the VISI was operated in the peak mode for most of its observation time. The spectral mode operation was carried out only several times a day to calibrate the peak mode data. From the spectral mode data, the intensity of an emission line can be derived by fitting a Gaussian to the pixel count and calculating the area under the Gaussian curve to integrate the photons of the O<sub>2</sub> emission band. Using spectral mode data obtained without contamination from moonlight and city light, the relationship between the estimated intensity and the peak-to-bottom counts simulated in the spectral data can be statistically determined. We assumed the relation can be expressed as follows:

$$I = \alpha \Delta C + \text{offset}, \quad (1)$$

where  $I$  is the total intensity in Rayleigh.  $\Delta C$  is the difference between the peak count and the bottom count,  $\Delta C = C_{\text{peak}} - C_{\text{bottom}}$ .  $\alpha$  is a factor of proportionality, including information on optical efficiency, the quantum efficiency of the CCD, and exposure time. The offset is a constant value determined for each line of the CCD

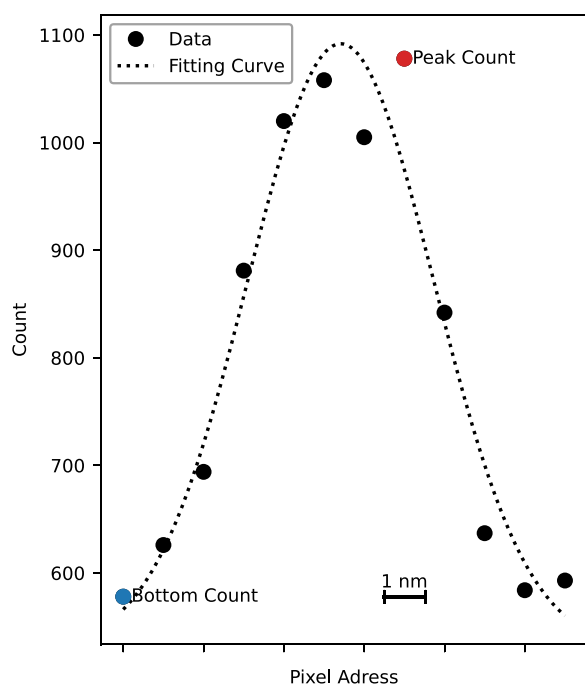


**Fig. 1** An example of the spectral mode data and peak mode data from VISI for the  $O_2(0-0)$  atmospheric band (762 nm), captured at 1803UT on April 16, 2018. In the spectral mode, all data in 12 pixels near an emission peak are downlinked. In the peak mode, only the maximum (peak) and minimum (bottom) count in the 12 pixels are downlinked. The dotted curve is a fitting Gaussian to the spectral mode data

and is basically a small value compared to typical values of  $\alpha\Delta C$ . In the process of bottom count subtraction ( $\Delta C = C_{\text{peak}} - C_{\text{bottom}}$ ), the contribution of the background light with a uniform spectrum is removed. Background lights having non-uniform spectrum components may still contaminate the VISI observations. The evaluation and removal of this contamination are crucial in this study and are described in detail in the next section.

The orbital inclination of the International Space Station is  $51.6^\circ$ . The latitudinal Coverage of the VISI observation is  $\pm 52^\circ$ . Image data of the  $O_2(0-0)$  airglow were mapped to an altitude plane at 95 km. At this mapping altitude, the swath width of FOV is  $\sim 670$  km. The spatial resolutions are 13 km along the orbit and 12–15 km perpendicular to it. The mapping algorithm of VISI image is detailed in Hozumi et al. (2018). Data from November 2012 to August 2015 were utilized to ascertain the global climatology of gravity wave activity.

## Methodology

The detection algorithm of gravity wave events and the methodology of occurrence analysis are described in this section. The basic idea of the approach in this study is similar to the method used by Hoffmann et al. (2013)

for detecting stratospheric gravity waves. We adapted the methodology for identifying mesospheric gravity waves in the VISI data. One of the key features of VISI is its dual FOVs; the forward and backward FOVs. By effectively using the data from these two FOVs, wave detection becomes more confident, and the observation coverage becomes wider. This section first outlines the wave detection and data screening algorithm using data from a single FOV. After that, the algorithm for combining two FOVs data is described.

### Wave detection algorithm

A 1D fit of a fourth-order polynomial is applied to each swath in the cross-track direction, and the fit is subtracted from the original image to retrieve small-scale perturbations. This subtraction serves two purposes, as with the AIRS in Hoffmann and Alexander (2010) and Hoffmann et al. (2013). The first is to remove an increase in radiance with an increasing line-of-sight angle in the sub-limb direction at the edge of the FOV. The second is to remove slowly varying background signals, e.g., those due to planetary-scale waves such as tides. Figure 2a shows examples of the original airglow intensity image from VISI  $O_2(0-0)$  band measurements on April 16, 2013, from 1126 to 1936UT. After subtracting the fourth-order polynomial fit, wave perturbations are visible, as shown in Fig. 2b. For example, wave perturbations are substantial over Myanmar to Laos, at longitudes  $90^\circ E$ – $110^\circ E$  and latitudes  $10^\circ N$ – $35^\circ N$ . A variance filter is then applied to the detrended airglow perturbations. For each data point, the variance  $\sigma^2$  of the airglow intensity of all data points within a distance  $r \leq 100$  km is calculated. Figure 2c shows the result of this variance filter. When the variance exceeds a threshold,  $\sigma^2 > \sigma_T^2$ , we define that gravity waves are present at the data point.

The threshold,  $\sigma_T^2$ , is determined as a function of the mean airglow intensity of all data points within a radius  $r \leq 100$  km, as shown below. The High-Resolution Doppler Imager (HRDI) on the Upper Atmosphere Research Satellite (UARS) indicated that the background intensity of  $O_2(0-0)$  band varies widely in longitude, even within the same latitude range, in each season (Hays 2003). The VISI data exhibit similar behavior. Setting the threshold as a function of the mean airglow intensity helps minimize the effect of the highly variable background in the wave occurrence analysis. The thresholds were determined separately for the forward and backward FOV data because the sensitivity and the instrumental noise differ depending on the FOV.

All intensity data with mapping points between  $130^\circ W$  and  $180^\circ W$  across all latitudes during moonless night conditions were collected to determine the threshold. The longitude range is recognized as relatively quiet in

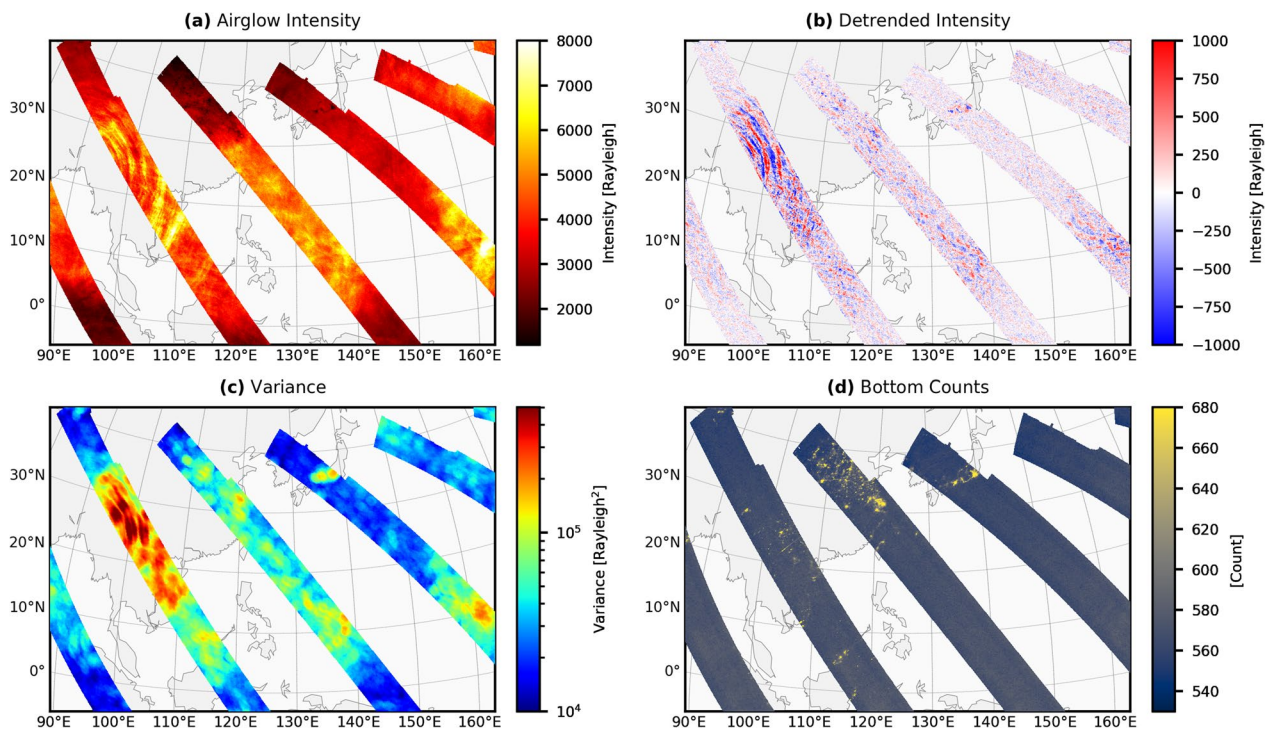


**Fig. 2** VISI O<sub>2</sub>(0-0) band measurements with the forward FOV on April 16, 2013, from 1126 to 1936UT. **a** Intensity of O<sub>2</sub>(0-0) band. **b** Perturbations of the airglow intensity as a result of the subtraction of a fourth-order polynomial fit. **c** Results of the variance analysis on O<sub>2</sub>(0-0) band measurements. **d** Bottom counts of the peak mode data. Images in **a–c** are mapped to the altitude plane of 95 km, and images in **d** are mapped to the ground

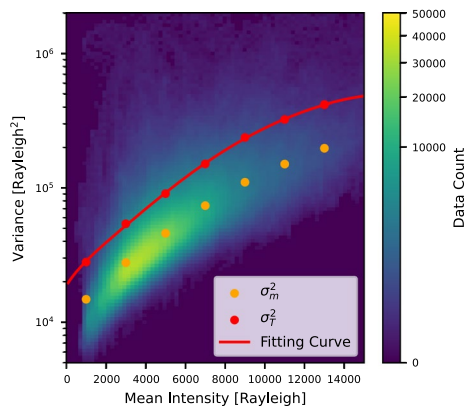


**Fig. 3** Histogram of data points as a function of mean intensity and variance. The data points from the forward FOV and observations in a longitude range from 130°W to 180°W. The mean variance,  $\sigma_m^2$ , and the variance threshold,  $\sigma_t^2$ , are indicated by orange and red dots, respectively. The red line indicates the fitting curve of  $\sigma_t^2$

terms of gravity wave activity, at least at stratospheric heights (Hoffmann et al. 2013). Since this region spans the Pacific Ocean, there are minimal city lights, thus reducing potential contamination sources for VISI observations. Figure 3 shows the histogram of data points

from the forward FOV as a function of mean intensity and variance. There are about 9 million data points from the forward FOV in the longitude over three years. The data were sorted into bins of mean intensity,  $I=0-2000$ ,  $2000-4000$ , ...,  $12,000-14,000$  Rayleigh. An initial variance threshold was calculated for each mean intensity bin as follows:

$$\sigma_I^2(I) = \sigma_m^2(I) + 3 \times \sqrt{\frac{1}{N-1} \sum_{i=1}^N [\sigma^2(I_i) - \sigma_m^2(I)]^2}, \quad (2)$$

where the mean variance  $\sigma_m^2(I)$  is defined by

$$\sigma_m^2(I) = \frac{1}{N} \sum_{i=1}^N \sigma^2(I_i), \quad (3)$$

with  $N$  referring to the number of data per mean intensity bin. Next, data with an intensity variance exceeding this initial threshold were excluded from the data set. The process of Eqs. (2) and (3), along with the data set updates, were iterated until the threshold converged to a certain value. After 22 iterations, the thresholds for all intensity ranges converged. The final variance threshold was determined for each mean intensity bin.

A fourth-order polynomial fit was applied to these variance thresholds. The fitting curve was used as the threshold for the occurrence analysis. The variance thresholds and the fitting curve are presented by red dots and a red line, respectively, in Fig. 3. The coefficients of polynomial fitting are summarized in Table 1. A negligible fraction of data exhibits a mean intensity above 14,000 Rayleigh (e.g., only 0.3% for the forward FOV data). Data up to 14,000 Rayleigh were evaluated against the threshold curve, while data exceeding this mean intensity were excluded from the occurrence analysis. The instrumental noise of the O<sub>2</sub>(0-0) band observation is estimated to be on the order of 100 Rayleigh, implying that wave signals surpassing the variance threshold significantly exceed the instrumental noise.

By applying the variance filter with a circular range of  $r=100$  km, this method effectively detects waves with a horizontal wavelength of 200 km or less. The lower limit of the detectable wavelength is determined by the instrument resolution, which is approximately 25 km. Since the double of  $1/e$  width of the O<sub>2</sub>(0-0) band airglow layer is  $\sim 10$  km (Burrage et al. 1994; Yee et al. 1997), the measurement is sensitive to waves with a vertical wavelength longer than 10 km. Overall, this method is primarily sensitive to waves with a horizontal wavelength ranging from 25 to 200 km and a vertical wavelength longer than 10 km.

$$\begin{aligned} \sigma^2 &= \frac{1}{n} \sum_{i=1}^n (I_{pi} - \bar{I}_p)^2 \\ &= \frac{\alpha^2}{n} \sum_{i=1}^n \{(\Delta C_{airglow,i} + \Delta C_{background,i}) - (\Delta \bar{C}_{airglow} + \Delta \bar{C}_{background})\}^2 \\ &= \alpha^2 \left\{ \sigma^2(\Delta C_{airglow}) + \sigma^2(\Delta C_{background}) + 2Cov(\Delta C_{airglow}, \Delta C_{background}) \right\}, \end{aligned} \tag{5}$$

**Table 1** The coefficients of polynomial fitting for the variance threshold

FOV	The coefficients of polynomial fitting				
	$a_4$	$a_3$	$a_2$	$a_1$	$a_0$
Forward	$-1.50 \times 10^{-11}$	$3.12 \times 10^{-7}$	$3.20 \times 10^{-4}$	7.35	$2.11 \times 10^4$
Backward	$-1.14 \times 10^{-11}$	$2.92 \times 10^{-7}$	$2.88 \times 10^{-5}$	12.2	$2.81 \times 10^4$

### Data screening algorithm

The VISI is a nadir-looking instrument, and its measurements can be affected or interfered with by contamination sources such as city lights and moonlight refractions from cloud tops or grounds, similar to VIIRS. There is strong absorption at the O<sub>2</sub>(0-0) band (762 nm) by O<sub>2</sub> below the emission height (Greenblatt et al. 1990), which significantly reduces the effects of city lights and moonlight refraction on VISI's O<sub>2</sub>(0-0) band measurements. However, when city lights or moonlight refractions are significant, the contamination is not negligible. For example, in Fig. 2c, the result of the variance filter shows larger values over the island of Japan. Nevertheless, in Fig. 2a and b, there is no wave signature in either the original intensity image or the detrend image upon visual inspection over Japan. This increase in variance is attributed to contamination by the city lights of Japan. Figure 2d shows the bottom counts of the peak mode data, highlighting city light contaminations in high-population areas, including Japan.

We express intensity perturbation,  $I_p$ , as consisting of two parts:

$$I_p = \alpha \Delta C_{airglow} + \alpha \Delta C_{background} \tag{4}$$

Here,  $\alpha \Delta C_{airglow}$  represents the part due to the emission peak of O<sub>2</sub>(0-0) band in this case. The background-contributed part,  $\alpha \Delta C_{background}$ , arises from non-uniform spectral components of background light, such as city lights or moonlight reflection. The variance used for the wave detection can be expressed as:

where  $n$  refers to the number of data points within  $r \leq 100$ km, and variables with bars denote the average value within the region.  $Cov(\Delta C_{airglow}, \Delta C_{background})$  represents the covariance of  $\Delta C_{airglow}$  and  $\Delta C_{background}$ . Since  $\Delta C_{airglow}$  and  $\Delta C_{background}$  are considered to have no correlation,  $Cov(\Delta C_{airglow}, \Delta C_{background})$  is approximately zero. Therefore, the variance can be expressed by the two components:

$$\sigma^2 \cong \alpha^2 \sigma^2(\Delta C_{\text{airglow}}) + \alpha^2 \sigma^2(\Delta C_{\text{background}}) \quad (6)$$

In the case  $\alpha^2 \sigma^2(\Delta C_{\text{background}})$  becomes large, the variance  $\sigma^2$  is contaminated and should be excluded from the dataset. Conversely, when  $\alpha^2 \sigma^2(\Delta C_{\text{background}})$  is negligibly small, the observed variance  $\sigma^2$  is attributed purely to the airglow perturbations.

The bottom counts of the peak mode data contain information on the intensity of background light. Figure 2d shows the image of bottom counts mapped to the ground, highlighting the distribution of city lights, the primary source of contamination. By calculating the variance of the bottom count  $\sigma^2(C_{\text{bottom}})$ , we assess the contribution of  $\sigma^2(\Delta C_{\text{background}})$  to the overall variance  $\sigma^2$ .  $\sigma^2(C_{\text{bottom}})$  is calculated by applying a high-pass filter with a fourth-order polynomial fitting, followed by a variance filter to the  $C_{\text{bottom}}$  data, the same as the process for the peak intensity data.  $C_{\text{bottom}}$  contains contributions from both uniform and non-uniform spectral components of background light, whereas  $\Delta C_{\text{background}}$  contains only non-uniform spectral components, owing to the subtraction process of the peak

mode data. Consequently, the bottom count variance is generally larger than the background contributed variance,  $\sigma^2(C_{\text{bottom}}) \geq \sigma^2(\Delta C_{\text{background}})$ . Despite this discrepancy, the bottom count variance,  $\sigma^2(C_{\text{bottom}})$ , serves as a reliable indicator of intensity of background contamination. In the case that  $\alpha^2 \sigma^2(C_{\text{bottom}})$  exceeds the variance threshold  $\sigma_T^2(I)$ ,

$$\alpha^2 \sigma^2(C_{\text{bottom}}) > \sigma_T^2(I) \quad (7)$$

We define that the background contributed variance is significant, and the data point is considered contaminated. Since the threshold,  $\sigma_T^2(I)$ , increases with the mean airglow intensity, some fluctuation in background light is acceptable at higher mean intensities. However, at lower mean intensities, even minor fluctuations in background light are deemed contaminative.

Moonlight refraction from cloud tops or the grounds is another significant source of contamination for VISI measurements. To filter out data strongly impacted by moonlight, we employ the illumination intensity defined by Ellis (1966), which is a relative value of the illumination received from the moon, ranging from 0 for no

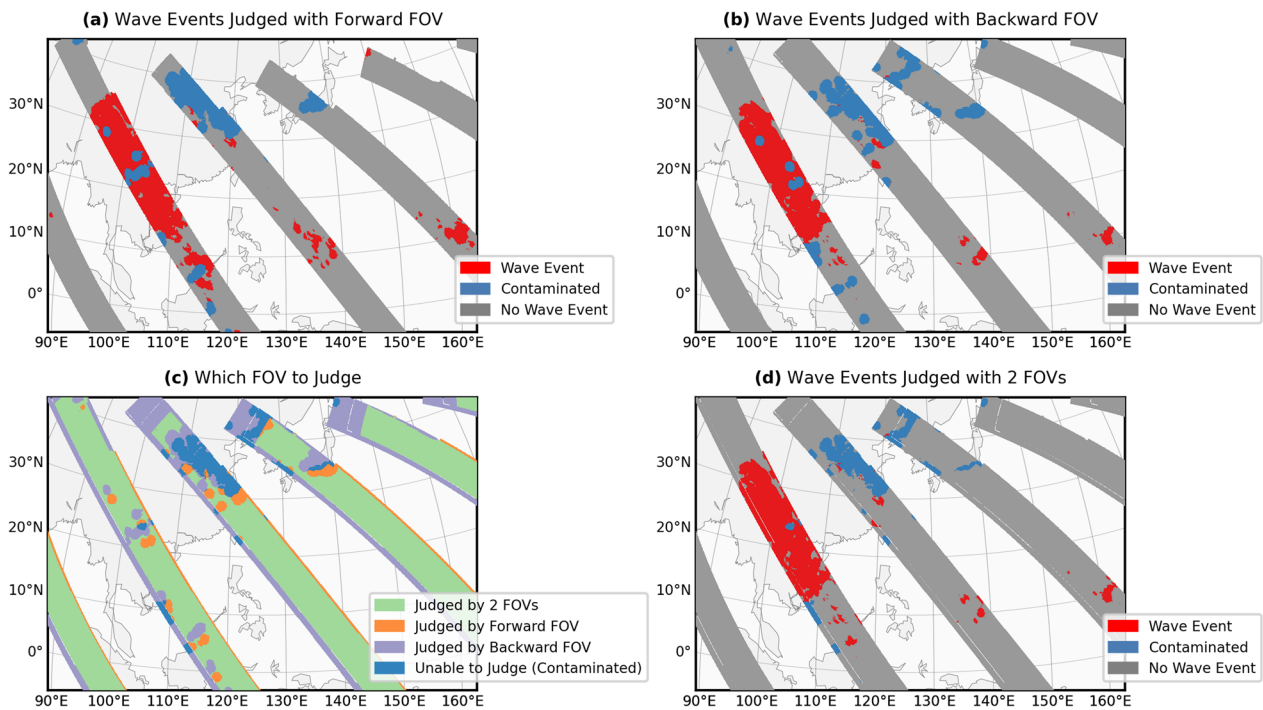


**Fig. 4** Results of wave event detection from the threshold analysis and data screening using the background variance for the forward FOV (a) and the backward FOV (b). The data period is as same as that of Fig. 2. c Indicates which FOV(s) are used to judge wave events. The green hatches (Judged by 2 FOVs) correspond to the situation of case #1 in Table 2. The orange hatches (judged by forward FOV) correspond to cases #3 & #5, the purple hatches (judged by backward FOV) correspond to cases #2 & #7, and the blue hatches (unable to judge) correspond to case #4, #6 & #8. d Shows the results of wave event detection from the combined use of two FOVs

moonlight to 100 for the full moon at the zenith. For the analysis of wave event occurrences, only data with an illumination intensity of 10 or less were considered. This criterion, in conjunction with the data screening algorithm, effectively mitigates the contamination effects caused by moonlight.

**Examples and combining algorithm of two FOVs data**

Figure 4a and b shows the results of the wave detection and data screening for the forward and backward FOV data, respectively. The data period is the same as that of Fig. 2. Red hatches denote regions where the variance exceeds the threshold, i.e., wave events are present, while gray hatches denote regions where the variance does not exceed the threshold, i.e., no wave events are present. Blue hatches indicate regions identified as contaminated based on the criteria of Eq. (7). Wave signatures over Myanmar to Laos are recognized as wave events in both FOV datasets. Fluctuations over the Pacific Ocean and the South China Sea are also considered wave events. The measurements are contaminated by city lights from Japan, China, and other Southeast Asian countries and are consequently filtered out using the criteria of Eq. (7).

A region in the airglow layer measured by the forward FOV of VISI is also measured by the backward FOV with a time difference, as illustrated in Fig. 5. The time difference,  $\Delta t$ , is about 90 s for the  $O_2(0-0)$  band, whose typical emission height is  $\sim 95$  km. Assuming that this time difference is short compared to the time scale of the temporal variation of wave distribution, it can be considered that the same region is measured twice by both the forward and backward FOV. In the case that the twice measurements are achieved (the case of Fig. 5a), a “double-check” filter is applied for wave detection.  $\sigma_F^2 > \sigma_{F.T}^2$  and  $\sigma_B^2 > \sigma_{B.T}^2$  are the criteria for identifying a wave event. Here, the subscript of “F.” (“B.”) indicates that the variable is for the forward (backward) FOV data. The double-check filter reduces the possibility of false positives and improves the robustness of the wave detection algorithm. In most parts of the observation coverage, the twice measurements are achieved (the green hatched area in Fig. 4c).

However, the twice measurements are not always available. When one FOV data set is contaminated, only the other FOV data is used for judgment. Due to the angle difference of the line of sight and the

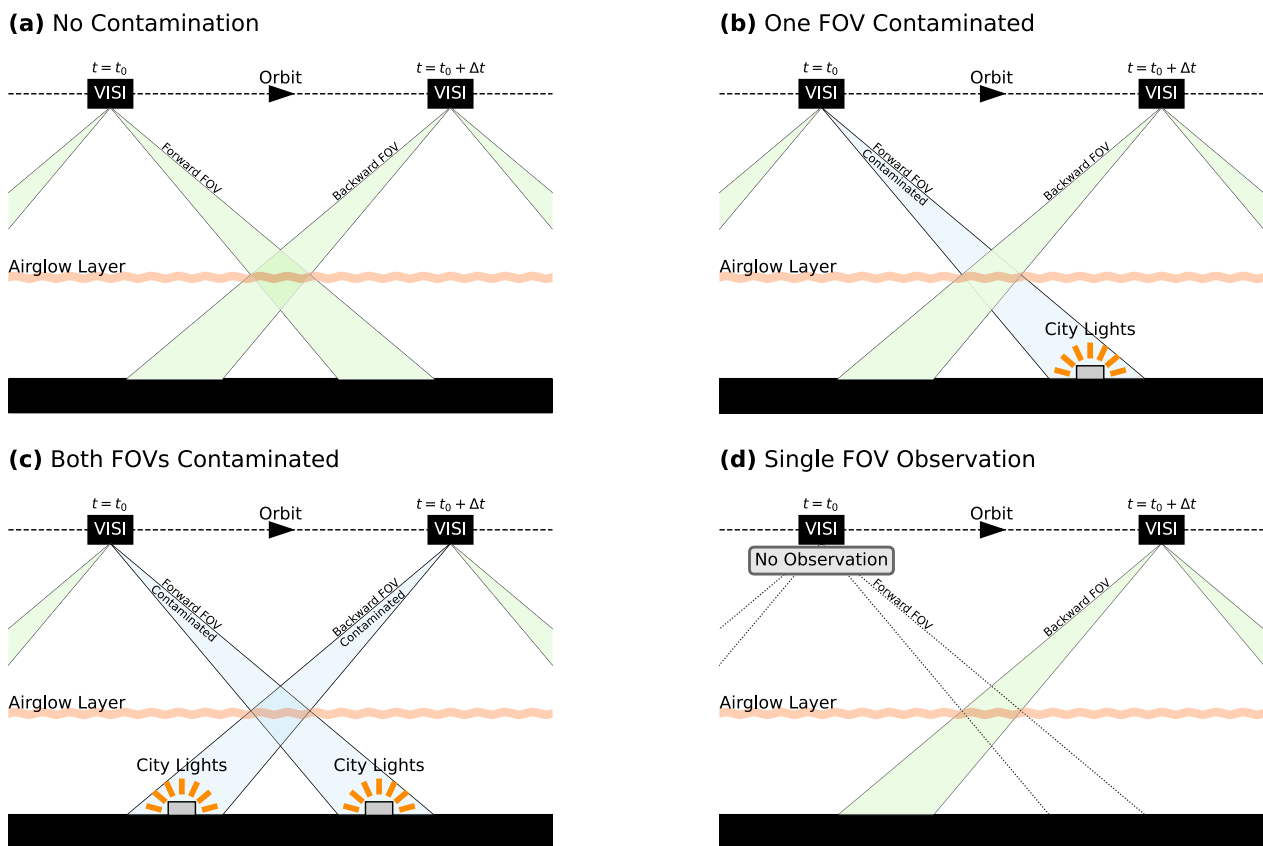


**Fig. 5** Schematic pictures explaining the stereoscopic observation of VISI with the forward and backward FOVs. The situations of a, b, c, and d correspond to cases of #1, #2, #4, and #7 of Table 2, respectively

height difference between the airglow emission and contamination sources, a contamination source with a limited area affects only one set of FOV data. The schematic picture of this situation is shown in Fig. 5b. When the forward FOV is contaminated, the criterion for identifying a wave event is  $\sigma_{B.}^2 > \sigma_{B.T.}^2$ , and vice versa. In Fig. 4c, orange (purple) hatches indicate areas where a wave event judgment is based on forward (backward) FOV data. Focusing on the vicinity of Japan in Fig. 4, the south of Japan is evaluated using forward FOV data, and the north of Japan is assessed with backward FOV data. This is because city light contamination is projected in different areas at the airglow altitude, depending on the viewing angle of each FOV.

When contamination sources are distributed in a wider area, both FOVs become contaminated. This situation is illustrated in Fig. 5c, where no clean data are available, rendering wave detection judgment impossible. For

example, city lights widely distributed over China result in contamination of both FOV data sets, as indicated by blue hatches in Fig. 4c.

There are additional scenarios where only a single FOV measurement is available: at the edge of the FOV swath and at the beginning and end of each orbital pass. When the ISS passes through the terminator and flies into the night side of Earth, VISI begins observing with both FOVs simultaneously. However, during the initial phase of each observation, the region observed by the backward FOV lacks a corresponding observation by the forward FOV, as illustrated in Fig. 5d. As will be obvious, in cases of single FOV measurement, the available single FOV data is utilized for the wave detection judgment. If this single data set is contaminated, judgment becomes impossible. In Fig. 4c, it is evident that measurements at the start of each observation are conducted only by the backward FOV.

**Table 2** Wave detection criteria depending on the measurement situation

Case #	Forward FOV measurement	Backward FOV measurement	Forward FOV NOT contaminated	Backward FOV NOT contaminated	Wave detection criteria
1	✓	✓	✓	✓	Judged by two FOVs
2	✓	✓	✓		Judged by forward FOV
3	✓	✓		✓	Judged by backward FOV
4	✓	✓			Contaminated
5	✓		✓		Judged by forward FOV
6	✓				Contaminated
7		✓		✓	Judged by backward FOV
8		✓			Contaminated

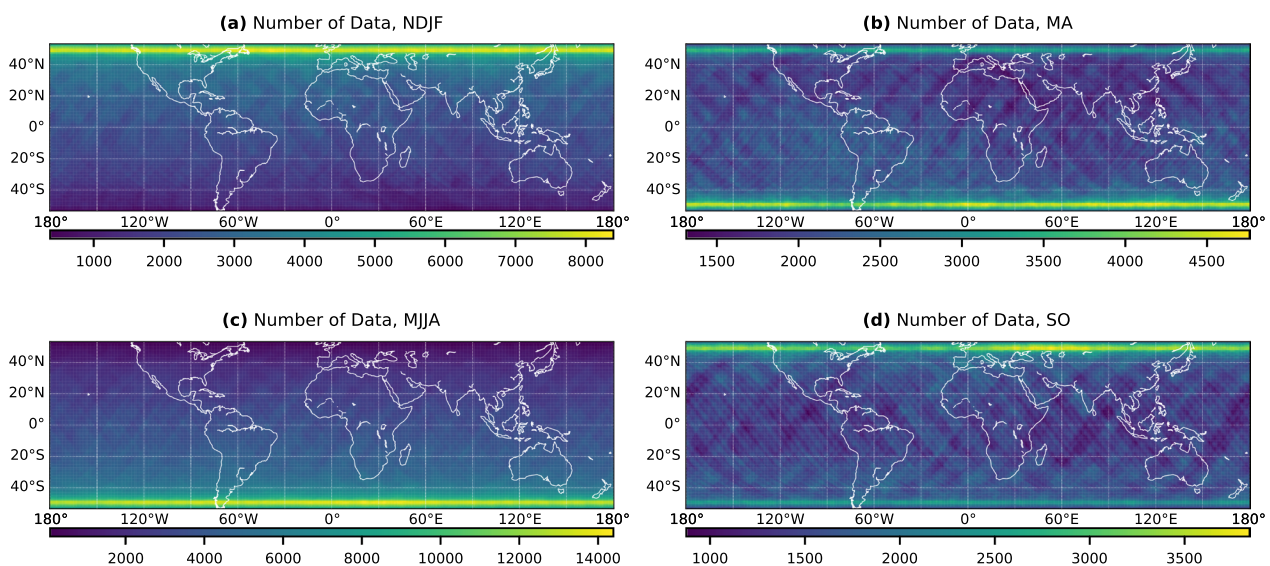


**Fig. 6** Number of data per  $1^\circ \times 1^\circ$  longitude–latitude bin for **a** November to February, **b** March and April, **c** May to August, and **d** September and October

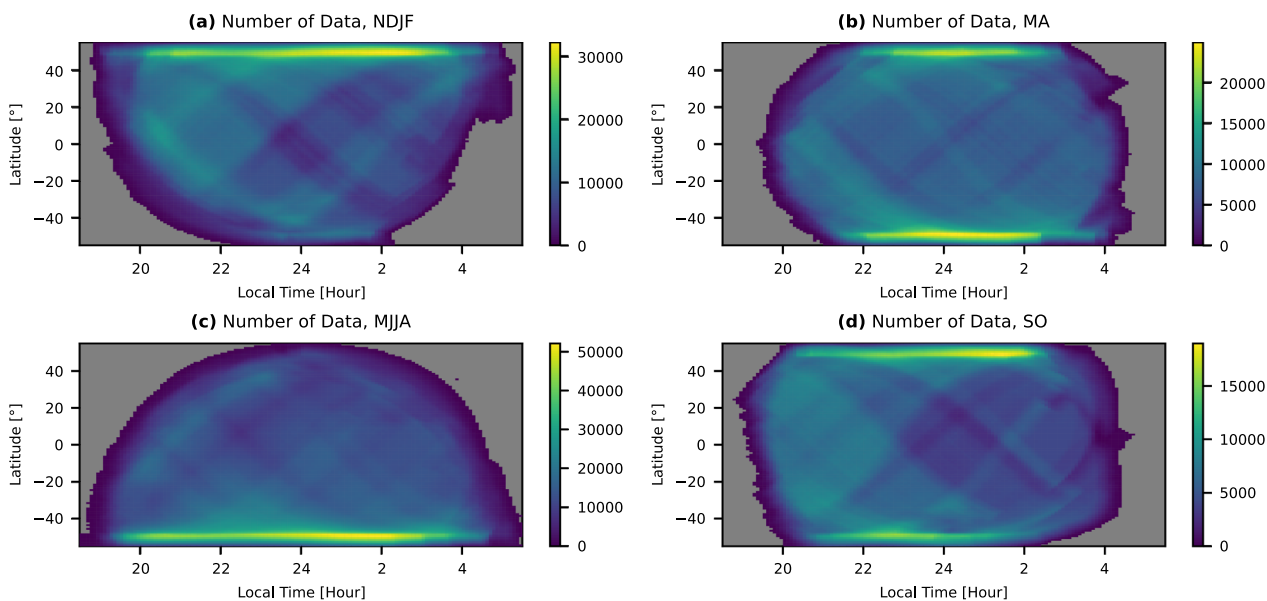


**Fig. 7** Number of data per 1° latitude by 5-min local time bin for the four seasons

The criteria for wave detection employed in this study are summarized in Table 2. Figure 4d shows the result of wave detection using data from both FOVs. Compared to the result from single FOV data, as shown in Fig. 4a and b, the contaminated areas are reduced because the two FOV data compensate for each other.

**Results**

By applying the detection method to the nearly three-year data set from VISI, frequency maps of gravity wave events were derived for four different seasons: November to February (NDJF), March and April (MA), May to August (MJJA), and September and October (SO). The occurrence frequency was calculated with 1° × 1° longitude–latitude bins. Figure 6 shows the number of data samples in each bin for the four seasons, including those

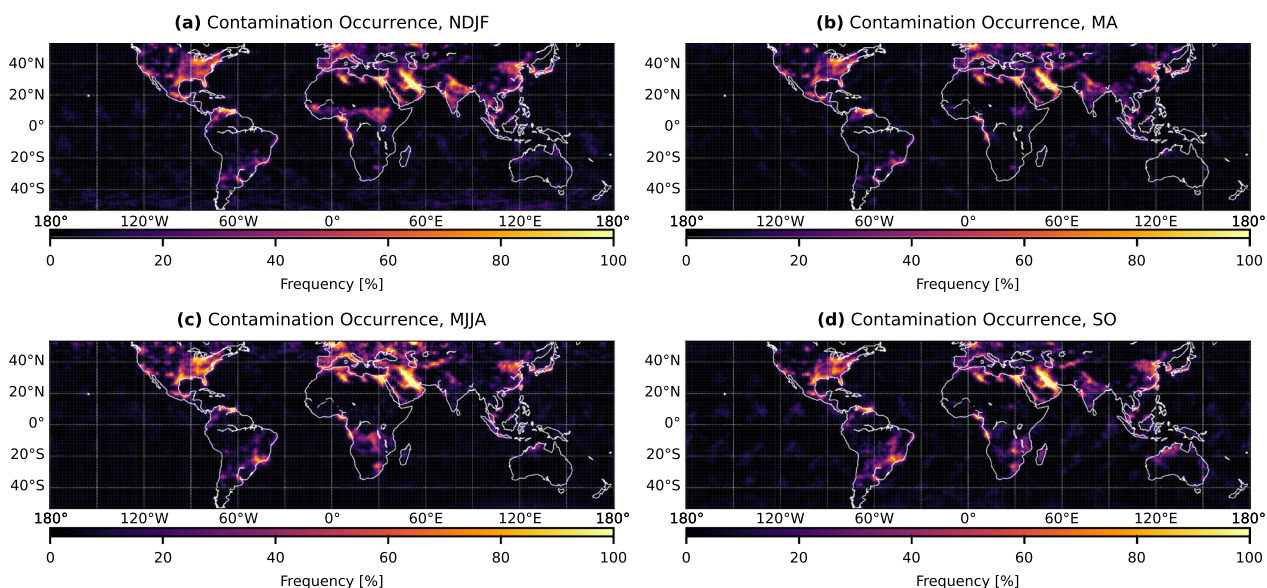


**Fig. 8** Occurrence frequency of data samples judged as contaminated

contaminated by background light. Approximately 50 data samples from one orbital pass contribute to a bin, meaning the number of unique orbital passes per bin is about 1/50th of the total shown in Fig. 6. Figure 7 shows the number of data per 1° latitude by 5-min local time bin, showcasing the local time coverage of the observations as a function of latitude for each season. Since VISI observations were made only at night, the number of data samples decreases and the local time coverage shortens at the summer high latitudes, where nighttime hours are fewer.

Figure 8 shows the occurrence frequency of data samples identified as contaminated. The judgment of contamination corresponds to cases #4, #6, and #8 in Table 2. The occurrence map of contamination correlates well with the distribution of city lights, confirming that city lights are a major contamination source (NASA/Goddard Space Flight Center, Scientific Visualization Studio, Earth’s City Lights, 2012). There are some seasonal variations in the contamination frequency. For example, contaminations are observed in the center of the African continent, between 0°–10° N during NDJF, and 0°–20° S during MJJA, with less contamination is noted in MA and SO. The seasonal variations can be attributed to the varying threshold. The threshold varies as a function of airglow intensity that changes in seasons (Burrage et al. 1994). A dim airglow situation provides conditions where even faint city lights result in contamination. The contamination map would be helpful to know relatively clean regions for nadir measurements of the O<sub>2</sub>(0-0) band. For

example, it is expected to be useful when considering calibration positions for future observation missions.

The occurrence frequency, defined as the percentage ratio of wave events to uncontaminated data samples, for each 1°×1° longitude–latitude bin and season, is presented in Fig. 9. Longitude–latitude bins with a contamination frequency exceeding 30% are considered difficult to show a proper wave occurrence; thus, they are masked with gray hatches in the figures. The occurrence maps are contaminated by aurora at longitudes of 70° E–170° E and latitudes higher than 40° S, where the magnetic latitude is relatively higher. Aurora signal yields a large variance of the VISI image. This is not excluded by the data screening algorithm of this study, which primarily focuses on eliminating contamination from sources below, such as city lights.

### Discussion

In Fig. 9, we observe several interesting features, which we will discuss in the following three sub-sections. The first sub-section focuses on the winter middle to high-latitude enhancement, likely related to the polar night jet and orographic hot spots. The second sub-section addresses enhancements in the summer hemisphere from the equator to high latitudes, likely associated with deep convection. The final sub-section discusses hot spots observed during the equinox seasons.

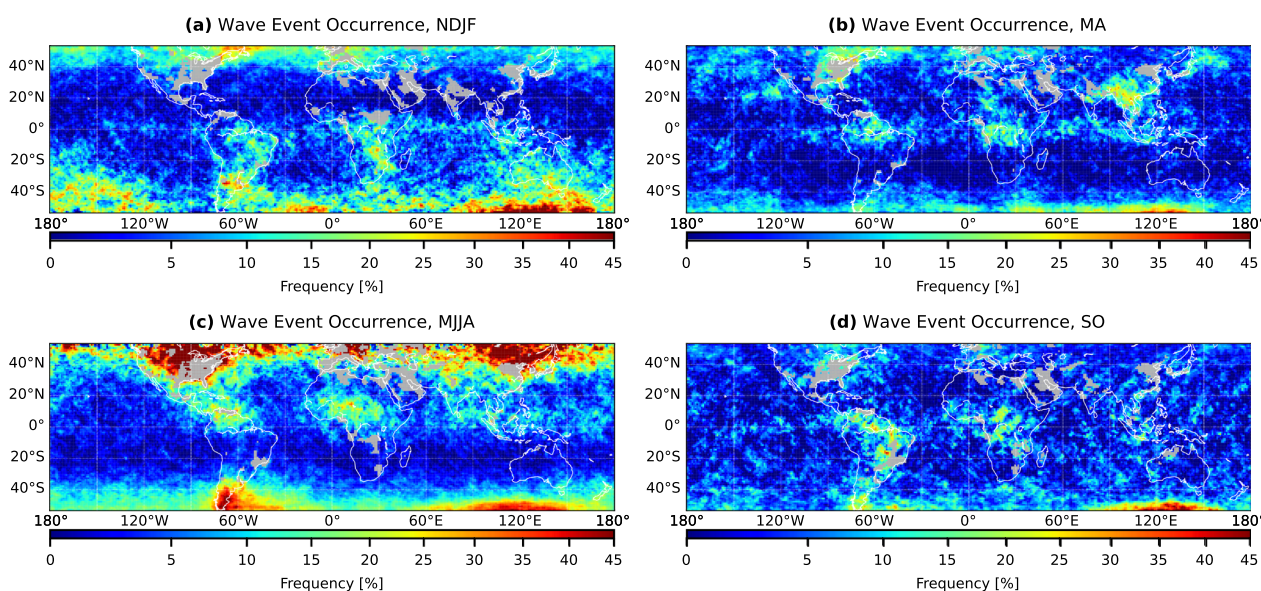


**Fig. 9** Wave event frequency from VISI observation from November 2012 to August 2015. Longitude–latitude bins with a contamination frequency exceeding 30% are masked with gray hatches

### Wave occurrence at winter middle to high latitudes

The polar vortex is known as an important source of gravity waves. Strong westerly winds of the jet permit the upward propagation of orographically generated gravity waves and other waves with westward intrinsic horizontal phase speeds, such that they avoid critical level filtering and propagate to higher altitudes before breaking. Recent studies have shown that these waves break in the stratosphere or lower mesosphere and generate higher-order gravity waves (Becker and Vadas 2018; Vadas et al. 2018; Vadas and Becker 2019). Secondary or high-order waves can then propagate the upper mesosphere and thermosphere (Vadas and Becker 2019; Vadas et al. 2019; Becker et al. 2022b; Harvey et al. 2023). The polar night jet is also known as a source of gravity waves by imbalance of the jet (O'Sullivan and Dunkerton 1995; Becker et al. 2022a). Gravity waves generated by imbalance also generate secondary GWs where they break (Vadas et al. 2023). Previous observations show strong gravity wave activity near the polar night jet, especially over the region where the wind is fastest, at the stratosphere and lower and middle mesosphere (Wu and Waters 1996; Wang and Alexander 2009; Jiang et al. 2006; Hoffmann et al. 2014, 2017; Ern et al. 2018; Hindley et al. 2020; Harvey et al. 2023). At the mesopause altitude, our results in Fig. 9 show a high occurrence of gravity wave activity at winter high latitudes ( $>40^\circ$  N/S in Fig. 9a and c) and are consistent with these previous observations.

During NDJF, in the high latitude of the Northern Hemisphere, the longitudinal sector from North America to Europe ( $100^\circ$  W– $30^\circ$  E) shows a particularly high occurrence compared to the region from the east of the Eurasian continent to the West Pacific ( $60^\circ$  E– $180^\circ$  E). Previous observations in the stratosphere and lower mesosphere reported a similar longitudinal structure of gravity wave activity (Alexander et al. 2009; Hoffmann et al. 2014, 2017; Harvey et al. 2023). This longitudinal enhancement of wave activity can be attributed to the zonal wave pattern of the jet that has faster eastward winds from North America to Europe. In the longitudinal band of higher occurrence, the occurrences over Europe and the east side of Canada are especially high. These hot spots are likely due to the orographically generated gravity waves. AIRS observations showed orographic hot spots in the stratosphere over the European Alps (Hoffmann et al. 2013) and the east side of Canada (Labrador, Hoffmann et al. 2017) during NDJF.

During MJJA, the winter high latitude between  $70^\circ$  E and  $170^\circ$  E experiences aurora contamination. Therefore, large-scale longitudinal patterns are difficult to examine there. However, a few hot spots are visible in the southern high latitude. A prominent hot spot over the southern Andes is caused by mountain waves due to wind flow

over the Andes and the Antarctic Peninsula. This region is where previous global measurements have shown higher wave activity in the stratosphere and mesosphere (e.g., Eckermann and Preusse 1999; Alexander et al. 2008; Wu and Eckermann 2008; Preusse et al. 2009; Ern et al. 2011; Hoffmann et al. 2013), and in the thermosphere as well (Park et al. 2014; Trinh et al. 2018; Vadas et al. 2019; Vadas and Becker 2019). The hot spot around the southern Andes is extended especially to the east with a zonal extension larger than  $40^\circ$ . Sato et al. (2012) explained that mountain waves can propagate leeward (eastward) due to advection by the background mean wind component perpendicular to the wavenumber vector. Vadas and Becker (2018) reported that mountain wave events were swept leeward due to the acceleration of the wind in time. The eastward extension of the hotspot in VISI can be attributed to these mechanisms.

We can see slightly higher occurrences around New Zealand and Tasmania, likely orographic hot spots, as they are known as a source of orographic gravity waves (Eckermann et al. 2016; Fritts et al. 2016).

### Wave occurrence related to convective gravity waves in the summer hemisphere

In NDJF and MJJA, middle to high latitudes in the summer hemisphere exhibit high wave occurrence. These middle to high-latitude maxima show distinct longitudinal variations. In NDJF, longitudinal maxima are observed over the Pacific Ocean ( $180^\circ$  W– $130^\circ$  W), South America to South Africa, and around Australia. In MJJA, two strong longitudinal maxima appear over North America and the east side of the Eurasian continent, and a third weaker maximum appears over Europe. A possible source of these maxima is deep convection in the middle to high-latitude summer. Over the North American Great Plains, it is known that thunderstorms, known as mesoscale convective systems, develop and generate a gravity wave hot spot during summer, May to August (Hoffmann et al. 2013). Previous imaging observations of mesospheric airglow often report wave signatures just above strong convective activity (e.g., Yue et al. 2009, 2013; Vadas et al. 2012; Akiya et al. 2014). Deep convection over the continents has different characteristics from those over the open ocean. AIRS showed a higher occurrence of deep convection and gravity wave events over the continents than over the oceans at summer middle latitudes (Hoffmann et al. 2013). This difference between continents and open ocean could lead to the three-peaked longitudinal structure of wave occurrence.

Another possible source that might contribute to the middle to high-latitude enhancements is horizontally propagated gravity waves originating from deep convection at equatorial latitudes (Forbes et al.

2021). Low-frequency gravity waves generated in the intertropical convection zone (ITCZ) are thought to propagate poleward in the summer hemisphere as they propagate upward (Sato et al. 2009). The latitudinal propagation is observed in limb-sounding measurements of the stratosphere and mesosphere (Ern et al. 2011) and demonstrated in simulations (Sato et al. 2009; Preusse et al. 2009). The three-peaked longitudinal structures of the summer middle to high latitudes maxima closely resemble those observed in the stratosphere and the lower and middle mesosphere (Ern et al. 2011), although our results exhibit some smearing compared to observations at lower altitudes. Ern et al. (2011) reported that the latitude of maxima in the summer hemisphere was at 30°–40° S/N in January and July of 2006 at an altitude of 70 km. The latitude of maxima in wave event occurrence in our results, at an altitude of around 95 km, appears to be shifted more poleward at ~40°–50° S/N or higher, although determining the exact latitude of maxima is challenging due to the limited latitudinal coverage of the VISI measurements (the latitudinal range of the occurrence map is 53° S–53° N).

During NDJF and MJJA, hotspots are found not only at middle to high latitudes, but also at low latitudes directly above the ITCZ. In NDJF, occurrences over Brazil (0°–30° S, 70° W–40° W), the south of the African continent (0°–30° S, 20° E–40° E), and the Maritime Continent/Australia (0°–30° S, 100° E–130° E) are high. In MJJA, occurrences over the north of South America (0°–20° N, 80° W–50° W), the middle of the African continent (0°–20° N, 0° E–30° E), and the Indian Ocean/the Maritime Continent (0°–20° N, 80° E–130° E) are high. These three peaks correspond well with the hot spots of deep convective plumes in the ITCZ (Vadas et al. 2014). These occurrence peaks are likely due to deep convective gravity waves from the ITCZ.

Previous global observations from limb-sounding instruments showed only poleward propagating waves (Ern et al. 2011). VISI, a nadir-viewing instrument, also shows wave activity at the mesopause above deep convection because it has a sensitivity to high-frequency waves with short horizontal wavelengths.

### Hot spots in the equinox seasons

Hot spots during the equinox seasons are relatively blurry compared to those of the solstice seasons. This is partially because of the relatively shorter date range of equinox data seasons. Since many hot spots or active regions during the equinox seasons are seen near previously known hot spots, we can speculate their source from their location.

During MA, hot spots are observed over the Amazon Rainforest, Congo Rainforest, Marin continent, the eastern part of North America, and the Indochina peninsula. They could be gravity wave hot spots from deep convection.

The hot spot over the Indochina peninsula is especially prominent and likely attributed to strong convective activity near the Bay of Bengal. An example of a wave event over the Indochina peninsula is shown in Fig. 2. Perwitasari et al. (2016) also highlighted the same event and identified the center of the concentric wave structures within the Bay of Bengal using VISI data. They also identified strong convective activity in the troposphere near the estimated center, which is the most likely source of the waves, with Three-hourly Tropical Rainfall Measuring Mission (TRMM) data. The occurrence analysis of AIRS stratospheric wave event showed a hot spot over the Bay of Bengal to Bangladeshi during MA (Hoffmann et al. 2013). Our results show that the hot spot has a large area with its edge about 1800 km east of the Bay of Bengal. This is reasonable because concentric waves in the mesosphere typically have a maximum radius of 600 km to 1800 km (Perwitasari et al. 2016).

During SO at equatorial latitudes, hot spots are observed over the Amazon Rainforest and the Congo Rainforest. They could be deep convection hot spots. The hot spot over the Marin continent is less prominent than those observed in other seasons. The occurrence over the southern Andes is high in SO. It could be an orographic hot spot related to the Andes and Antarctic Peninsula, which in general runs from May to October (Liu et al 2019).

### Summary

The global climatology of gravity wave activity across four seasons was derived from nearly three years of VISI data on the O<sub>2</sub>(0-0) band emission. To detect gravity wave events, we evaluated the variance of high-pass filtered O<sub>2</sub> band images within a local 100 km radius. We applied a variance threshold for the detection, three times the standard deviation from the average variance of the background level as shown in Eq. (2), varying as a function of the background mean airglow brightness. VISI's nadir-viewing measurements of O<sub>2</sub>(0-0) band emission are contaminated by upwelling city light emissions, especially over highly populated areas. The data screening algorithm using bottom counts of peak mode data effectively removed contaminated data.

The occurrence maps show a higher frequency of wave events in winter high latitudes (>40° N/S), which can be attributed to gravity wave activity associated with the polar night jet, which generates gravity waves

and amplifies gravity waves from sources below the jet. In winter high latitudes, hot spots were observed near orographic sources, including the eastern part of North America, Europe, the southern Andes, New Zealand, and Tasmania. In the summer middle to high latitudes, higher wave occurrences with three longitudinal maxima were detected. We speculate they are due to gravity waves from deep convection that arise from mid-latitude summertime thunderstorms. Additionally, horizontally propagated gravity waves originating from deep convection at the ITCZ could contribute to this middle to high-latitude enhancement. Hot spots were identified just above the ITCZ, likely due to high-frequency waves propagating vertically from deep convection. During the equinox seasons, hot spots were noted in the vicinity of strong convection regions, including the Amazon Rainforest, Congo Rainforest, the Marin continent, the eastern part of North America, and the Indochina peninsula. They are presumed to be convective hotspots. An orographic hot spot was also observed over the southern Andes during SO.

The global analysis can provide valuable information for future local studies with ground-based observations to interpret local results in a global context. Our results clearly show the potential of space-born imaging of O<sub>2</sub>(0–0) band emission in global observation of small-scale waves (horizontal wavelength of ~25–200 km) in the upper mesosphere around 95 km. It can fill the observational gap between the stratosphere and thermosphere and offers a useful dataset for investigating wave activity on a global scale.

#### Abbreviations

VISI	Visible and near-Infrared Spectral Imager
IMAP	Ionosphere, Mesosphere, upper Atmosphere and Plasmasphere
ISS	International Space Station
LIMS	Limb Infrared Monitor of the Stratosphere
GPS	Global Positioning System
CRISTA	Cryogenic Infrared Spectrometers and Telescopes for the Atmosphere
MLS	Microwave Limb Sounder
HIRDLS	High Resolution Dynamics Limb Sounder
SABER	Sounding of the Atmosphere using Broadband Emission Radiometry
AIRS	Atmospheric Infrared Sounder
CIPS	Cloud Imaging and Particle Size
DNB	Day–Night Band
VIIRS	Visible/Infrared Imaging Radiometer Suite
Suomi NPP	Suomi National Polar-orbiting Partnership
FOV	Field-of-View
HRDI	High-Resolution Doppler Imager
UARS	Upper Atmosphere Research Satellite
NDJF	November, December, January and February
MA	March and April
MJJA	May, June, July and August
SO	September and October
TEC	Total electron content
TRMM	Three Hourly Tropical Rainfall Measuring Mission

#### Acknowledgements

Data used in this study are from the Ionosphere, Mesosphere, upper Atmosphere, and Plasmasphere mapping mission from the ISS (ISS-IMAP mission). The authors express their gratitude to the two anonymous reviewers whose constructive and insightful comments significantly contributed to the enhancement of this manuscript, particularly improving the discussion section.

#### Author contributions

YH, AS, and JY conceived the study. YH developed the wave detection technique. AS led the ISS-IMAP mission. AS, TS, and AY developed VISI instruments. TS, AS, and YH processed and calibrated VISI data. YH, JY, and HL interpreted the results from a scientific perspective. All authors read and approved the final manuscript.

#### Funding

This work was supported by JSPS KAKENHI Grant Numbers JP24403008. YH and JY were supported by the NASA grant 80NSSC22K0641 and ONR RAM-HORNS N00014-21-1-2112.

#### Availability of data and materials

ISS-IMAP/VISI data will be available on Data ARchives and Transmission System (DARTS) of ISAS/JAXA (<https://www.darts.isas.jaxa.jp/stp/imap/data.html>). ISS-IMAP/VISI data are also available via e-mail inquiry to Akinori Saito at Kyoto University ([saitoua@kugi.kyoto-u.ac.jp](mailto:saitoua@kugi.kyoto-u.ac.jp)).

#### Declarations

##### Ethics approval and consent to participate

Not applicable.

##### Consent for publication

Not applicable.

##### Competing interests

The authors declare that they have no competing interests.

#### Author details

<sup>1</sup>National Institute of Information and Communications Technology, Tokyo, Japan. <sup>2</sup>Present Address: The Catholic University of America, Washington, DC, USA. <sup>3</sup>NASA Goddard Space Flight Center, Greenbelt, MD, USA. <sup>4</sup>Graduate School of Science, Kyoto University, Kyoto, Japan. <sup>5</sup>Planetary Plasma and Atmospheric Research Center, Tohoku University, Sendai, Japan. <sup>6</sup>Institute of Space and Astronautical Science, Japan Aerospace Exploration Agency, Sagami, Japan. <sup>7</sup>High Altitude Observatory, National Center for Atmospheric Research, Boulder, CO, USA.

Received: 5 July 2023 Accepted: 8 March 2024

Published online: 07 May 2024

#### References

- Akiya Y, Saito A, Sakanoi T, Hozumi Y, Yamazaki A, Otsuka Y, Nishioka M, Tsugawa T (2014) First spaceborne observation of the entire concentric airglow structure caused by tropospheric disturbance. *Geophys Res Lett* 41(19):6943–6948. <https://doi.org/10.1002/2014gl061403>
- Alexander MJ, Pfister L (1995) Gravity wave momentum flux in the lower stratosphere over convection. *Geophys Res Lett* 22(15):2029–2032. <https://doi.org/10.1029/95gl01984>
- Alexander MJ, Gille J, Cavanaugh C, Coffey M, Craig C, Eden T, Francis G, Halvorson C, Hannigan J, Khosravi R, Kinnison D, Lee H, Massie S, Nardi B, Barnett J, Hepplewhite C, Lambert A, Dean V (2008) Global estimates of gravity wave momentum flux from High Resolution Dynamics Limb Sounder observations. *J Geophys Res* 113(D15):1–11. <https://doi.org/10.1029/2007jd008807>
- Alexander SP, Klekociuk AR, Tsuda T (2009) Gravity wave and orographic wave activity observed around the Antarctic and Arctic stratospheric vortices by the COSMIC GPS-RO satellite constellation. *J Geophys Res Atmos*. <https://doi.org/10.1029/2009jd011851>

- Becker E, Vadas SL (2018) Secondary gravity waves in the winter mesosphere: results from a high-resolution global circulation model. *J Geophys Res Atmos* 123(5):2605–2627. <https://doi.org/10.1002/2017jd027460>
- Becker E, Goncharenko L, Harvey VL, Vadas SL (2022a) Multi-step vertical coupling during the January 2017 sudden stratospheric warming. *J Geophys Res Space Phys*. <https://doi.org/10.1029/2022ja030866>
- Becker E, Vadas SL, Bossert K, Harvey VL, Zülicke C, Hoffmann L (2022b) A high-resolution whole-atmosphere model with resolved gravity waves and specified large-scale dynamics in the troposphere and stratosphere. *J Geophys Res Atmos*. <https://doi.org/10.1029/2021jd035018>
- Burrage MD, Arvin N, Skinner WR, Hays PB (1994) Observations of the O<sub>2</sub> atmospheric band nightglow by the high resolution Doppler imager. *J Geophys Res* 99(A8):15017–15017. <https://doi.org/10.1029/94ja00791>
- Eckermann SD, Preusse P (1999) Global measurements of stratospheric mountain waves from space. *Science* 286:1534–1537
- Eckermann SD, Broutman D, Ma J, Doyle JD, Pautet P-D, Taylor MJ, Bossert K, Williams BP, Fritts DC, Smith RB (2016) Dynamics of Orographic gravity waves observed in the mesosphere over the Auckland islands during the deep propagating gravity wave experiment (DEEPWAVE). *J Atmos Sci* 73(10):3855–3876. <https://doi.org/10.1175/jas-d-16-0059.1>
- Ellis DC (1966) Illumination received from the moon. *J R Astron Soc Canada* 60:221
- Ern M (2004) Absolute values of gravity wave momentum flux derived from satellite data. *J Geophys Res*. <https://doi.org/10.1029/2004jd004752>
- Ern M, Preusse P, Gille JC, Hepplewhite CL, Mlynczak MG, Russell JM, Riese M (2011) Implications for atmospheric dynamics derived from global observations of gravity wave momentum flux in stratosphere and mesosphere. *J Geophys Res Atmos* 116(19):1–24. <https://doi.org/10.1029/2011JD015821>
- Ern M, Hoffmann L, Preusse P (2017) Directional gravity wave momentum fluxes in the stratosphere derived from high-resolution AIRS temperature data. *Geophys Res Lett* 44(1):475–485. <https://doi.org/10.1002/2016gl072007>
- Ern M, Trinh QT, Preusse P, Gille JC, Mlynczak MG, Russell JM, Riese M (2018) GRACLE: a comprehensive climatology of atmospheric gravity wave parameters based on satellite limb soundings. *Earth Syst Sci Data* 10(2):857–892. <https://doi.org/10.5194/essd-10-857-2018>
- Fetzer EJ, Gille JC (1994) Gravity wave variance in LIMS temperatures. Part I: variability and comparison with background winds. *J Atmos Sci* 51(17):2461–2483
- Forbes JM, Zhang X, Randall CE, France J, Harvey VL, Carstens J, Bailey SM (2021) Troposphere-mesosphere coupling by convectively forced gravity waves during southern hemisphere monsoon season as viewed by AIM/CIPS. *J Geophys Res Space Phys*. <https://doi.org/10.1029/2021ja029734>
- Fritts DC, Alexander MJ (2003) Gravity wave dynamics and effects in the middle atmosphere. *Rev Geophys*. <https://doi.org/10.1029/2001RG000106>
- Fritts DC, Smith RB, Taylor MJ, Doyle JD, Eckermann SD, Dörnbrack A, Rapp M, Williams BP, Pautet PD, Bossert K, Criddle NR, Reynolds CA, Reinecke PA, Uddstrom M, Revell MJ, Turner R, Kaifler B, Wagner JS, Mixa T, Kruse CG, Nugent AD, Watson CD, Gisinger S, Smith SM, Lieberman RS, Laughman B, Moore JJ, Brown WO, Haggerty JA, Rockwell A, Stossmeister GJ, Williams SF, Hernandez G, Murphy DJ, Klekociuk AR, Reid IM, Ma J (2016) The Deep Propagating Gravity Wave Experiment (DEEPWAVE): an airborne and ground-based exploration of gravity wave propagation and effects from their sources throughout the lower and middle atmosphere. *Bull Am Meteor Soc* 97(3):425–453. <https://doi.org/10.1175/bams-d-14-00269.1>
- Greenblatt GD, Orlando JJ, Burkholder JB, Ravishankara AR (1990) Absorption measurements of oxygen between 330 and 1140 nm. *J Geophys Res*. <https://doi.org/10.1029/JD095iD11p18577>
- Harvey VL, Randall CE, Goncharenko LP, Becker E, Forbes JM, Carstens J, Xu S, France JA, Zhang SR, Bailey SM (2023) CIPS observations of gravity wave activity at the edge of the polar vortices and coupling to the ionosphere. *J Geophys Res Atmos*. <https://doi.org/10.1029/2023jd038827>
- Hays PB (2003) A global view of the molecular oxygen night airglow. *J Geophys Res* 108(D20):4646–4646. <https://doi.org/10.1029/2003JD003400>
- Hindley NP, Wright CJ, Hoffmann L, Moffat-Griffin T, Mitchell NJ (2020) An 18-year climatology of directional stratospheric gravity wave momentum flux from 3-D satellite observations. *Geophys Res Lett*. <https://doi.org/10.1029/2020gl089557>
- Hoffmann L, Alexander MJ (2010) Occurrence frequency of convective gravity waves during the North American thunderstorm season. *J Geophys Res Atmos* 115(20):1–14. <https://doi.org/10.1029/2010JD014401>
- Hoffmann L, Xue X, Alexander MJ (2013) A global view of stratospheric gravity wave hotspots located with Atmospheric Infrared Sounder observations. *J Geophys Res Atmos* 118(2):416–434. <https://doi.org/10.1029/2012jd018658>
- Hoffmann L, Alexander MJ, Clerbaux C, Grimsdell AW, Meyer CI, Rößler T, Tournier B (2014) Intercomparison of stratospheric gravity wave observations with AIRS and IASI. *Atmos Meas Tech* 7(12):4517–4537. <https://doi.org/10.5194/amt-7-4517-2014>
- Hoffmann L, Spang R, Orr A, Alexander MJ, Holt LA, Stein O (2017) A decadal satellite record of gravity wave activity in the lower stratosphere to study polar stratospheric cloud formation. *Atmos Chem Phys* 17(4):2901–2920. <https://doi.org/10.5194/acp-17-2901-2017>
- Holton JR (1982) The role of gravity wave induced drag and diffusion on the momentum budget of the mesosphere. *J Atmos Sci* 39(4):791–799
- Holton JR (1983) The influence of gravity wave breaking on the general circulation of the middle atmosphere. *J Atmos Sci* 40(10):2497–2507
- Hozumi Y, Saito A, Sakanoi T, Yamazaki A, Hosokawa K (2018) Mesospheric bores at southern midlatitudes observed by ISS-IMAP/MSI: a first report of an undulating wave front. *Atmos Chem Phys* 18(22):16399–16407. <https://doi.org/10.5194/acp-18-16399-2018>
- Hozumi Y, Saito A, Sakanoi T, Yamazaki A, Hosokawa K, Nakamura T (2019) Geographical and seasonal variability of mesospheric bores observed from the international space station. *J Geophys Res Space Physics* 124:3775–3785. <https://doi.org/10.1029/2019JA026635>
- Jiang JH, Eckermann SD, Wu DL, Wang DY (2006) Inter-annual variation of gravity waves in the Arctic and Antarctic winter middle atmosphere. *Adv Space Res* 38(11):2418–2423. <https://doi.org/10.1016/j.asr.2005.09.036>
- Lindzen RS (1981) Turbulence and stress owing to gravity wave and tidal breakdown. *J Geophys Res* 86(C10):9707–9707. <https://doi.org/10.1029/JC086iC10p09707>
- Liu X, Xu J, Yue J, Vadas SL, Becker E (2019) Orographic primary and secondary gravity waves in the middle atmosphere from 16-year SABER observations. *Geophys Res Lett* 46(8):4512–4522. <https://doi.org/10.1029/2019gl082256>
- Miller SD, Mills SP, Elvidge CD, Lindsey DT, Lee TF, Hawkins JD (2012) Suomi satellite brings to light a unique frontier of nighttime environmental sensing capabilities. *Proc Natl Acad Sci USA* 109(39):15706–15711. <https://doi.org/10.1073/pnas.1207034109>
- Miller SD, Straka WC 3rd, Yue J, Smith SM, Alexander MJ, Hoffmann L, Setvak M, Partain PT (2015) Upper atmospheric gravity wave details revealed in nightglow satellite imagery. *Proc Natl Acad Sci USA* 112(49):E6728–E6735. <https://doi.org/10.1073/pnas.1508084112>
- Nastrom GD, Fritts DC (1992) Sources of mesoscale variability of gravity waves. Part I: topographic excitation. *J Atmos Sci* 49(2):101–110
- O'Sullivan D, Dunkerton TJ (1995) Generation of inertia-gravity waves in a simulated life cycle of Baroclinic instability. *J Atmos Sci* 52(21):3695–3716. [https://doi.org/10.1175/1520-0469\(1995\)052%3C3695:GOIWA%3E2.0.CO;2](https://doi.org/10.1175/1520-0469(1995)052%3C3695:GOIWA%3E2.0.CO;2)
- Park J, Lühr H, Lee C, Kim YH, Jee G, Kim JH (2014) A climatology of medium-scale gravity wave activity in the midlatitude/low-latitude daytime upper thermosphere as observed by CHAMP. *J Geophys Res Space Phys* 119(3):2187–2196. <https://doi.org/10.1002/2013ja019705>
- Perwitasari S, Sakanoi T, Nakamura T, Ejiri MK, Tsutsumi M, Tomikawa Y, Otsuka Y, Yamazaki A, Saito A (2016) Three years of concentric gravity wave variability in the mesopause as observed by IMAP/MSI. *Geophys Res Lett* 43:11528–11535. <https://doi.org/10.1002/2016gl071511>
- Plougonven R, Zhang F (2014) Internal gravity waves from atmospheric jets and fronts. *Rev Geophys* 52(1):33–76. <https://doi.org/10.1002/2012rg000419>
- Preusse P, Eckermann SD, Ern M, Oberheide J, Picard RH, Roble RG, Riese M, Russell JM, Mlynczak MG (2009) Global ray tracing simulations of the SABER gravity wave climatology. *J Geophys Res*. <https://doi.org/10.1029/2008jd011214>
- Randall CE, Carstens J, France JA, Harvey VL, Hoffmann L, Bailey SM, Alexander MJ, Lumpe JD, Yue J, Thuraijagah B, Siskind DE, Zhao Y, Taylor MJ, Russell JM (2017) New AIM/CIPS global observations of gravity waves near 50–55 km. *Geophys Res Lett* 44(13):7044–7052. <https://doi.org/10.1002/2017gl073943>

- Sakanoi T, Akiya Y, Yamazaki A, Otsuka Y, Saito A, Yoshikawa I (2011) Imaging observation of the earth's mesosphere, thermosphere and ionosphere by VISI of ISS-IMAP on the international space station. *IEEJ Trans Fundam Mater* 131(12):983–988. <https://doi.org/10.1541/ieejfms.131.983>
- Sato K, Watanabe S, Kawatani Y, Tomikawa Y, Miyazaki K, Takahashi M (2009) On the origins of mesospheric gravity waves. *Geophys Res Lett* 36(19):1–5. <https://doi.org/10.1029/2009GL039908>
- Sato K, Tateno S, Watanabe S, Kawatani Y (2012) Gravity wave characteristics in the southern hemisphere revealed by a high-resolution middle-atmosphere general circulation model. *J Atmos Sci* 69(4):1378–1396. <https://doi.org/10.1175/jas-d-11-0101.1>
- Trinh QT, Ern M, Doornbos E, Preusse P, Riese M (2018) Satellite observations of middle atmosphere-thermosphere vertical coupling by gravity waves. *Ann Geophys* 36(2):425–444. <https://doi.org/10.5194/angeo-36-425-2018>
- Tsuda T, Nishida M, Rocken C, Ware RH (2000) A global morphology of gravity wave activity in the stratosphere revealed by the gps occultation data (GPS/MET). *J Geophys Res Atmos* 105(D6):7257–7273. <https://doi.org/10.1029/1999JD901005>
- Vadas SL, Becker E (2018) Numerical modeling of the excitation, propagation, and dissipation of primary and secondary gravity waves during wintertime at McMurdo station in the Antarctic. *J Geophys Res Atmos* 123(17):9326–9369. <https://doi.org/10.1029/2017jd027974>
- Vadas SL, Becker E (2019) Numerical modeling of the generation of tertiary gravity waves in the mesosphere and thermosphere during strong Mountain wave events over the Southern Andes. *J Geophys Res Space Physics* 124(9):7687–7718. <https://doi.org/10.1029/2019ja026694>
- Vadas S, Yue J, Nakamura T (2012) Mesospheric concentric gravity waves generated by multiple convective storms over the North American Great Plain. *J Geophys Res Atmos*. <https://doi.org/10.1029/2011jd017025>
- Vadas SL, Liu HL, Lieberman RS (2014) Numerical modeling of the global changes to the thermosphere and ionosphere from the dissipation of gravity waves from deep convection. *J Geophys Res Space Phys* 119(9):7762–7793. <https://doi.org/10.1002/2014ja020280>
- Vadas SL, Zhao J, Chu X, Becker E (2018) The excitation of secondary gravity waves from local body forces: theory and observation. *J Geophys Res Atmos* 123(17):9296–9325. <https://doi.org/10.1029/2017jd027970>
- Vadas SL, Xu S, Yue J, Bossert K, Becker E, Baumgarten G (2019) Characteristics of the quiet-time hot spot gravity waves observed by GOCE over the southern Andes on 5 July 2010. *J Geophys Res Space Physics* 124(8):7034–7061. <https://doi.org/10.1029/2019ja026693>
- Vadas SL, Becker E, Bossert K, Baumgarten G, Hoffmann L, Harvey VL (2023) Secondary gravity waves from the stratospheric polar vortex over ALO-MAR observatory on 12–14 January 2016: observations and modeling. *J Geophys Res Atmos*. <https://doi.org/10.1029/2022jd036985>
- Wang L, Alexander MJ (2009) Gravity wave activity during stratospheric sudden warmings in the 2007–2008 Northern Hemisphere winter. *J Geophys Res Atmos*. <https://doi.org/10.1029/2009jd011867>
- Wu DL, Eckermann SD (2008) Global gravity wave variances from *Aura* MLS: characteristics and interpretation. *J Atmos Sci* 65(12):3695–3718. <https://doi.org/10.1175/2008JAS2489.1>
- Wu DL, Waters JW (1996) Satellite observations of atmospheric variances: a possible indication of gravity waves. *Geophys Res Lett* 23(24):3631–3634. <https://doi.org/10.1029/96gl02907>
- Yee J-H, Crowley G, Roble RG, Skinner WR, Burrage MD, Hays PB (1997) Global simulations and observations of O(1 S), O 2 (1  $\Sigma$ ) and OH mesospheric nightglow emissions. *J Geophys Res* 102(A9):19949–19949. <https://doi.org/10.1029/96JA01833>
- Yue J, Vadas SL, She CY, Nakamura T, Reising SC, Liu HL, Stamus P, Krueger DA, Lyons W, Li T (2009) Concentric gravity waves in the mesosphere generated by deep convective plumes in the lower atmosphere near Fort Collins, Colorado. *J Geophys Res Atmos* 114(6):1–12. <https://doi.org/10.1029/2008JD011244>
- Yue J, Hoffmann L, Joan Alexander M (2013) Simultaneous observations of convective gravity waves from a ground-based airglow imager and the AIRS satellite experiment. *J Geophys Res Atmos* 118(8):3178–3191. <https://doi.org/10.1002/jgrd.50341>
- Yue J, Perwitasari S, Xu S, Hozumi Y, Nakamura T, Sakanoi T, Saito A, Miller SD, Straka W, Rong P (2019) Preliminary Dual-Satellite observations of

atmospheric gravitywaves in airglow. *Atmosphere*. <https://doi.org/10.3390/atmos10110650>

## Publisher's Note

Springer Nature remains neutral with regard to jurisdictional claims in published maps and institutional affiliations.